Nanoscale crystal fabric of primary Ediacaran dolomite

Julia Wilcots[1,1], Pupa U P A Gilbert[2,2], and Kristin D Bergmann[1,1]

[1]Massachusetts Institute of Technology
[2]University of Wisconsin

November 30, 2022

Abstract

Dolomite (CaMg(CO3)2) forms in minor quantities in few modern environments yet comprises most of the Precambrian carbonate rock record. Precambrian dolomites are often fine-grained and fabric-retentive and are interpreted to have precipitated as primary cements or formed as early diagenetic replacements of CaCO3. Primary dolomite precipitation from seawater in depositional environments has not yet been described. Here, we use synchrotron radiation to produce a nanoscale-resolution crystal orientation map of one exquisitely preserved ooid deposited at the onset of the Shuram carbon isotope excursion at ˜574 Ma. The crystal orientation map reveals small (˜10 μm) acicular, radially-oriented crystals grouped into bundles of similarly-oriented crystals with varying optical properties. We interpret this dolomite formed via primary, spherulitic precipitation during ooid growth in shallow marine waters. This result provides additional evidence that the physicochemical properties of late Precambrian oceans promoted dolomite precipitation and supports a primary origin for the Shuram excursion.

Nanoscale crystal fabric preserved in dolomite ooids at the onset of the Shuram Excursion

Julia Wilcots[1], Pupa U. P. A. Gilbert[2], Kristin D. Bergmann[1]

[1]Department of Earth, Atmospheric and Planetary Sciences, Massachusetts Institute of Technology, Cambridge, MA

[2]Departments of Physics, Chemistry, Materials Science, Geoscience, University of Wisconsin, Madison, WI

Key Points:

- Fabric-preserving ooids at the onset of the Shuram carbon isotope excursion are comprised of micron-sized, stoichiometric dolomite crystals
- Dolomite crystals are acicular, radially-oriented, and arranged in plumose spherulite-like bundles
- We interpret that this ooid formed as primary dolomite, with implications for seawater chemistry at the onset of the Shuram excursion

Corresponding author: Julia Wilcots, jwilcots@mit.edu

Abstract

Dolomite ($CaMg(CO_3)_2$) forms in minor quantities in modern environments yet comprises most of the Precambrian carbonate rock record. Precambrian dolomites are often fine-grained and fabric-retentive and are interpreted to have precipitated as primary cements or formed as early diagenetic replacements of $CaCO_3$. Detailed physical and chemical characterization of these dolomites could inform their origin and relevance for paleoenvironmental reconstruction. Here, we use synchrotron radiation to produce a nanometer-resolution crystal orientation map of one exquisitely-preserved ooid deposited at the onset of the Shuram carbon isotope excursion (∼574 Ma). The crystal orientation map reveals small (∼10µm) acicular, radially-oriented crystals grouped into bundles of similarly-oriented crystals with varying optical properties. We interpret that this dolomite formed via primary, spherulitic precipitation during ooid growth in shallow marine waters. This result provides additional evidence that the physicochemical properties of late Precambrian oceans promoted dolomite precipitation and supports a primary origin for the Shuram excursion.

Plain Language Summary

The mineral dolomite is a common constituent of ancient carbonate sedimentary rocks, yet dolomite rarely precipitates from seawater today. For decades, this discrepancy has caused researchers to wonder whether dolomite precipitated directly from seawater in the deep past. If so, dolomitic rocks — like other carbonate sedimentary rocks — could preserve the physical and chemical properties of the water from which they formed and serve as a record of ancient marine conditions. However, evidence for primary dolomite precipitation from seawater has not been described. Here, we apply a new method and study one 574 million-year-old dolomite at nanometer resolution using x-ray light, creating a three-dimensional map of crystals in this sample. We discover our sample is comprised of tiny, needle-shaped dolomite crystals that are arranged in bundles of similarly-oriented crystals. After comparison to modern primary and lab-grown dolomites and to other ancient dolomites, we interpret this crystal fabric to have formed via precipitation from seawater. Our discovery of a new dolomite crystal fabric and our interpretation that it precipitated from seawater shed new light on the ancient environment at the onset of Earth's largest carbon cycle perturbation.

1 Introduction

Carbonate rocks serve as the primary sink for carbon in the Earth system and preserve a record of the physical, chemical, and biological properties of marine settings throughout geologic time. The interpretation of the physical and chemical properties of carbonates

through Earth history elucidates past changes in climate and carbon cycling, and also provides insight into potential future changes to the Earth system. However, carbonates are susceptible to post-depositional, often cryptic, diagenetic alteration which can chemically or physically alter a carbonate mineral's composition and diminish a carbonate's usefulness as a paleoenvironmental proxy.

At ∼574 Ma, as animal life was emerging (Rooney et al., 2020), carbonate rocks on at least six paleocontinents preserve evidence for Earth's largest negative carbon isotope anomaly, known as the Shuram excursion (Derry, 2010; Fike et al., 2006; Grotzinger et al., 2011; Husson et al., 2020). Understanding whether the anomaly and the −12‰ $\delta^{13}C_{VPDB}$ values recorded at its nadir (Grotzinger et al., 2011) reflect a primary environmental perturbation or post-depositional processes is an ongoing geochemical and sedimentological challenge. Conventionally, carbonate carbon isotopes ($\delta^{13}C$) are understood as a global steady-state balance between the isotopic composition of a carbon source (i.e., the mantle) and carbon sinks (organic and carbonate carbon). Perturbations in $\delta^{13}C$ arise due to changes in the amount or isotopic composition of sources and sinks. For the case of the Shuram excursion, a global carbon cycle perturbation mechanism may have involved oxidizing a large pool of isotopically light organic (Rothman et al., 2003), or methane (Bjerrum & Canfield, 2011) carbon – mechanisms with implications for atmospheric pO_2 during Shuram time. Diagenetic or post-depositional hypotheses argue that such negative $\delta^{13}C$ values were caused as a result of fluid-rock interactions during late burial diagenesis (Derry, 2010), diagenetic meteoric waters depleted in $\delta^{13}C$ due to an active terrestrial biosphere (Knauth & Kennedy, 2009), or the precipitation of authigenic carbonates from non-seawater-like fluids (Schrag et al., 2013). In these scenarios, any primary environmental data would be overprinted by secondary alteration. Because the Shuram excursion is hosted in strata that also host early Ediacaran (635-539 Ma) biota and precedes the evolution of metazoans by < 20 Myr (Rooney et al., 2020), understanding the cause of the Shuram excursion and whether it represents a primary perturbation to the global carbon cycle has implications for how we understand the environments in which early animals evolved.

In this study, we approach the question of whether Shuram carbon isotope values are hosted in diagenetically-altered carbonates by analyzing the physical and chemical characteristics of a distinctive dolomite ooid grainstone that appears exquisitely fabric-preserving in thin section (Figure 2) and records the onset of the Shuram excursion ($\delta^{13}C$ = -2.8‰) in the upper Khufai Formation, Huqf outcrop area, Sultanate of Oman (see Table 3, sample MD6 258.6 in Bergmann et al. (2018)). Ooids are spherical carbonate grains that form a cortex surrounding an inner nucleus via precipitation from seawater. Because they form only in very shallow water high-energy settings, ooids serve as useful paleoenvironmental

indicators, and their tendency to preserve mineralogy-dependent crystal fabric makes them useful samples for petrographic analysis (Sandberg, 1975). The upper Khufai oolite is a stromatolite bioherm-bearing, 1-30m thick, cross-stratified ooid and intraclast grainstone that directly overlies mudstones containing evaporite pseudomorphs and is interpreted to have been deposited in a high-energy, shallow marine setting with elevated seawater sulfate concentrations (Figure 1, Osburn et al. (2014); Cui et al. (2021)).

Using x-ray diffraction (XRD), electron probe microanalysis (EPMA), and synchrotron-based nanoscale crystal orientation mapping, we reveal the mineralogy and crystal morphology (size, shape, arrangement) of the ca. 574 Ma upper Khufai oolite. We then interpret these observations in the context of previously proposed dolomitization models, laboratory experiments, and modern dolomite-forming environments. We assess whether this ooid precipitated as a diagenetic replacement of primary $CaCO_3$ or directly from seawater and discuss implications for the genesis of the Shuram excursion and properties of Precambrian shallow marine environments.

2 Results

To assess the mineralogy and fabric of the upper Khufai oolite, we analyzed portions of one $\sim$ 10cm$\times$10cm oolite sample using electron probe microanalyis (EPMA), x-ray diffraction (XRD), thin section microscopy, and Polarization-dependent Imaging Contrast (PIC) mapping (see Materials and Methods).

2.1 Mineralogy

Magnesium-to-Calcium ratios from EPMA (Fig. 2b) and the presence of the (015) and (021) ordering peaks (Kaczmarek et al., 2017) in the XRD spectrum (Fig. 2c) indicate that ooids are comprised of stoichiometric, ordered dolomite: Ca and Mg are present in equal parts within the carbonate lattice within coherent cation-specific planes. Elemental maps (Supplemental Figure 1) and thin section images (Figure 2d-f) show the ooids are loosely cemented by a dolomite cement bearing higher concentrations of Si than the ooids (Supplemental Figure 1c-d), and show Mn-rich concentric banding in the cortices of many ooids (Supplemental Figure 1b).

2.2 Fabric

We leverage the nanoscale resolution of synchrotron-based Polarization-dependent Imaging Contrast (PIC) mapping to produce a high-resolution map of crystal orientations and geometries within one ooid grain from the upper Khufai oolite (Figure 3). Using soft x-rays

with variable linear polarization angle, PIC mapping measures the c-axis orientations of nanocrystals and displays them in 3D, at 20nm resolution, using color: hue and brightness represent in- and out-of-plane angles, respectively (see Appendix A2 and Gilbert et al. (2011)). Since PIC mapping is based on x-ray linear dichroism — a physical effect that depends on bond angle orientation and crystal structure — its prior observation and use in aragonite, calcite, and vaterite (DeVol et al., 2014) suggests that it also works for dolomite, as demonstrated here for the first time.

PIC mapping reveals that this ooid's cortex is dominantly comprised of small, acicular (needle-shaped) dolomite crystals; dolomite crystals in the nucleus are generally larger and equant (Figure 3). We focus our analysis on the well-preserved fabric of the outer cortex, in which individual dolomite crystals are small ($\sim$ 2µm by 15µm), acicular, and radially oriented. Some crystals are grouped into bundles of similarly-oriented crystals; within bundles, crystal orientations span a range of just $\sim 60°$ (Fig. 3b, c, e). While crystals within each bundle maintain similar orientations (Fig. 3), the optical characteristics of crystals differ between bundles: some are length-fast, with the c-axes pointing along the same vector as the bundle (e.g., purple bundle, Fig. 3c), while others are length-slow, with the c-axes pointing perpendicular to the bundle orientation (e.g., green bundle, Fig. 3b). Each bundle has a curved, plumose morphology that becomes more expansive towards the edge of the ooid. This curvature is visible as a change in brightness, hue, or both across a given bundle (Figure 3e). Finally, most plumose spherulitic bundles terminate at the preserved curved outer edge of the ooid (labeled in Figure 3a).

3 Discussion

The small volumes of modern dolomite compared to the large volumes of geologic, and especially Precambrian ($>$ 541 Ma) dolomite (Given & Wilkinson, 1987; Cantine et al., 2020) has inspired decades of work aimed at determining the conditions that promote dolomite formation. The apparent abundance of dolomite in the late Precambrian that preserves finely crystalline and mimetic crystal fabrics (Corsetti et al., 2006; Hood et al., 2011; Hood & Wallace, 2018; Tucker, 1982, 1983) has prompted efforts focused explicitly on the question of how these fabric-retentive dolomites formed and why they abound in late Precambrian strata. Since geologic dolomite is predominantly a replacement of precursor $CaCO_3$, many dolomite-replacement studies have investigated the conditions under which fabric-preserving or mimetic dolomitization can occur and the resultant petrographic and geochemical qualities of these dolomitized calcium carbonates (e.g., Bullen & Sibley, 1984; Zempolich & Baker, 1993). But dolomite can also form as a primary precipitate under

laboratory experiments and in modern environments. Below we explore which formation mechanism best explains our observations of the upper Khufai oolite.

3.1 Mimetic dolomitization of primary $CaCO_3$

Mimetic dolomitization preserves the primary textures, or fabrics, of a precursor calcium carbonate. Most studies of mimetic dolomites invoke an "early diagenetic" or synsedimentary origin for the secondary dolomite (e.g., Hood & Wallace, 2018; Corsetti et al., 2006; Osburn et al., 2014; Zempolich & Baker, 1993), an interpretation derived from comparison to fabric-destructive (interpreted as late diagenetic) dolomites (e.g., Corsetti et al., 2006) and experimental results (Zempolich & Baker, 1993).

To characterize the nature of fabric-retentive Precambrian ooids, Zempolich and Baker (1993) dolomitized modern aragonitic ooids over 180 hours at 200°C. In these experiments, dolomitization begins at the outer surface of an ooid with the formation of a dolomite rind and progresses inward via micro pore spaces, replacing <µm primary $CaCO_3$ with euhedral, microrhombic (2-8µm) dolomite crystals (Zempolich & Baker, 1993). The precipitated dolomite crystals faithfully preserve the ooids' primary tangential macrostructure and overall shape (enveloped by a rind of euhedral dolomite crystals) but do not preserve their primary optical characteristics (pseudo-uniaxial cross), and appear distinctly rhombohedral in SEM images (Zempolich & Baker, 1993). In another mimetic dolomitization experiment, Bullen and Sibley (1984) dolomitized a range of skeletal materials and produced fine, but coarser than primary $CaCO_3$, crystal sizes in echinoids and preserved radial extinction in forams, but found similar coarse dolomite rhombs as Zempolich and Baker (1993) on the exterior of the fossils that protruded into pore space.

Our results highlight key differences with these dolomitization experiments (Zempolich & Baker, 1993; Bullen & Sibley, 1984). We see no evidence for an outer rind of euhedral dolomite crystals, which would be visible as a thin ring around the PIC mapped ooid (Figure 3a), nor do we observe replacement rhombs protruding into pore space. Dolomite crystals within the cortex of Khufai ooids are predominately acicular, not euhedral or rhombic, and are coherently organized into bundles of similarly-oriented crystals, preserving primary optical characteristics. There is also no evidence that replacement occurred from the outer edge of the ooid inwards. If dolomite did replace primary $CaCO_3$ in the Khufai, it did so via a different, and possibly novel mechanism capable of precipitating non-euhedral dolomite pseudomorphically, to preserve primary crystal orientations and thus optical properties.

3.2 Primary dolomite precipitation from seawater

To understand whether paleoenvironmental conditions could have promoted primary dolomite precipitation and the characteristics we observe in the upper Khufai Formation, we turn to reports of modern dolomite-forming environments and laboratory studies that successfully precipitate dolomite from solution. Dolomite can only be found forming as the primary carbonate mineral on Earth's surface today in small quantities in unique hypersaline, hydrothermal, lacustrine, or biologically-mediated environments. In the Coorong lakes of South Australia, fine grained (<1 µm - 20 µm), spherulitic dolomite precipitates during the hottest (> 30°C), most evaporitic portion of the year in high-salinity, high pH, high [Mg^{2+}] settings dominated by sulfate-reducing bacteria (Wacey et al., 2007). In Lagoa Vermelha, Brazil, Ca-rich dolomite with depleted $\delta^{13}C$ (-7.49 to -8.98 ‰) forms in anoxic, hypersaline conditions dominated by sulfate-reducing bacteria at the sediment-water interface (Vasconcelos & McKenzie, 1997; Vasconcelos et al., 2006). This primary precipitated dolomite then "ages" in the anoxic sediment column (<1m depth) to a more stoichiometric, ordered form (Vasconcelos & McKenzie, 1997; Vasconcelos et al., 2006). The presence of sulfur-reducing bacteria is thought to be critical to dolomite formation in both of these modern examples, and has been identified in laboratory studies as a potential mechanism (through the production of dissolved sulfide and subsequent disruption of Mg^{2+}-water complexes) for the precipitation of dolomite in the geologic record (Zhang et al., 2012; Fang, Zhang, et al., 2021).

Laboratory experiments support the observation that microbial mediation and disruption of Mg^{2+}-water complexes are important elements for dolomite precipitation. In experiments with anoxygenic photosynthetic microbes and Mn-enriched water, Daye et al. (2019) successfully precipitated ordered, nano- to micro-crystalline, Mn-enriched dolomite within biofilms. Recent abiotic experiments by Fang, Zhang, et al. (2021) and Fang and Xu (2022) demonstrate that disrupting the Mg^{2+}-water "hydration barrier" to free Mg^{2+} in solution is a critical step in precipitating primary dolomite from solution. In their experiments, disordered micrometer-scale dolomite is precipitated from a water-ethanol or a $Si(OH)_4$-rich solution at room temperature (Fang, Zhang, et al., 2021; Fang & Xu, 2022). As a final example, at high temperatures (60-200°C) and high dolomite supersaturation, Rodriguez-Blanco et al. (2015) precipitate protodolomite as nanocrystalline spherulites. These poorly ordered precursors transform to ordered dolomite comprised of larger (>100 nm), planar crystals over hours to days (Rodriguez-Blanco et al., 2015). Together, these studies demonstrate that, with the correct combination of biological or chemical factors, primary, ordered, nano- to microscale dolomite – all qualities of the upper Khufai dolomitic ooids – can precipitate as a primary carbonate mineralogy at Earth surface temperatures.

3.2.1 How do bundles of similarly-oriented crystals form?

Lastly, we seek an analogue or mechanism to explain the bundles of similarly-oriented crystals we observe in the outer cortex of our PIC mapped ooid (Figure 3b, c, e). In some ways, the PIC mapped bundles resemble the fascicular slow dolomite (FSD) cements described by Hood et al. (2011). These isopachous, length-slow dolomite crystals are arranged in bundles that fan outward, and are interpreted to represent primary dolomite cements precipitated in pore space in the early diagenetic environment of the ca. 650 Ma Balcanoona Reef Complex (Hood et al., 2011; Hood & Wallace, 2012). However, FSD cements are characterized by their length-slow crystal orientation, while our PIC map reveals bundles that are both length-fast and length-slow.

The bundles we observe, particularly the bundle shown in Figure 3b, nearly resemble plumose spherulites – feather-shaped bundles of crystal fibers that grow radially outward and have been observed and PIC mapped in aragonitic ($CaCO_3$) coral skeletons (Sun et al., 2017, 2021). The co-orientation of crystals (within 60°) we observe in each bundle (Figure 3b, c) are similar to the co-orientations Sun et al. (2017) observe in natural (coral) and synthetic aragonitic spherulites. However, true spherulites have a length-fast optical character and are space-filling. Our PIC mapped bundles are variably length-fast and length-slow, and not individually space-filling, although the bundles we identify together create a space-filling mosaic of acicular dolomite throughout the ooid's cortex.

The curvature across individual bundles, visible in the PIC map in Figure 3 as color gradients, shows that adjacent nanocrystals within each bundle are slightly misoriented with respect to one another, a characteristic of spherulites (Sun et al., 2017). Individual crystal orientations vary gradually, akin to the orientation of adjacent radii around a sphere. This observation of curvature, consistent across most bundles (Figure 3), indicates that these bundles of acicular, radially-oriented crystals had space to grow into as they formed (see, for example, Sun et al. (2017)).

3.3 A model for the formation of primary dolomitic ooids in the Khufai Formation

Based on the PIC map and petrographic data presented and discussed above, we propose a primary dolomite mineralogy for the fabric-preserving ooids of the upper Khufai Formation. The geologic and geochemical context (Osburn, 2013; Osburn et al., 2014; Cui et al., 2021) suggests microbial processes that increased alkalinity or $[Mg^{2+}]$ (Rodriguez-Blanco et al., 2015; Daye et al., 2019; Wacey et al., 2007), the presence of chemical species that disrupted Mg^{2+}-water complexes (Fang, Zhang, et al., 2021; Zhang et al., 2012), ele-

vated temperatures in shallow water environments (Bergmann et al., 2018), and hypersalinity (Wacey et al., 2007; Cui et al., 2021) could have individually or in tandem promoted dolomite formation within the upper Khufai oolite.

The large (> 1cm) size of some of the ooids in the upper Khufai oolite (Figure 2d, e), the radially-oriented crystals in each ooid's cortex, and evident concentric banding in many ooids (Figure 2b, e, f) fit the "bedform model" of ooid growth proposed by Anderson et al. (2020). In this model, developed to explain giant ooids in the sedimentary record, ooids grow while at rest in active bedforms and abrade during transport, forming concentric bands (see Trower et al. (2017) for an alternative growth model). Invoking this "bedform model," we suggest the upper Khufai ooids may have precipitated in pore spaces within the sediment pile of periodically active bedforms from seawater that was kinetically favorable for dolomite precipitation (Anderson et al., 2020).

Dolomite precipitation within each ooid's cortex may have proceeded spherulitically, either via non-crystallographic branching (Sun et al., 2017) or growth from randomly oriented "sprinkles" (possibly observed surrounding the ooid's nucleus in Figure 3a; Sun et al. (2021)). We cannot determine whether the dolomite precipitated as ordered dolomite (as in the experiments of (Daye et al., 2019)) or quickly "aged" to ordered dolomite (as observed by Vasconcelos et al. (1995) and Rodriguez-Blanco et al. (2015)).

The upper Khufai ooids were then partially cemented by Si-bearing dolomite cements (Supplemental Figure 1). Other upper Khufai sections are more thoroughly silica cemented and silicified (Osburn et al., 2014). Rapid silica cementation has been described in other Ediacaran strata as a symptom of high Si saturation in Ediacaran oceans (Tarhan et al., 2016) and dissolved silica has also been shown to promote dolomite precipitation by disrupting the Mg^{2+}-H_2O complexes in modern sediments and experiments (Fang, Hobbs, & Xu, 2021; Fang & Xu, 2022), suggesting the presence of Si may have been important for both precipitation and preservation of the upper Khufai Formation. The lack of pore-filling cements in our analyzed oolite may be an indication that post-depositional diagenetic fluids – which did produce fabric-destructive dolomitization in lower Khufai ooids elsewhere in Oman (Wright et al., 1990; Bergmann et al., 2018) – did not come in contact with this portion of the Khufai Formation. The fine-grained siliciclastic sediments of the overlying Shuram Formation may also have protected the upper Khufai Formation from later fluid alteration and cementation, and the ordered dolomite mineralogy of the ooids themselves likely made them more recalcitrant to alteration than metastable phases like aragonite and high Mg-calcite.

3.4 Implications for the Shuram excursion and Ediacaran environments

Our results support a primary origin for the Shuram excursion. We interpret the upper Khufai dolomitic ooids to have formed as primary precipitates from seawater and do not observe evidence for the precipitation of late diagenetic minerals, meaning most geochemical signals hosted by these ooids should reflect the seawater from which they precipitated. As has been discussed recently by carbonate sedimentologists working in modern and ancient sediments (Geyman & Maloof, 2019; Ahm & Husson, 2021), this does not require that seawater DIC at ∼574 Ma was globally depleted in ^{13}C. However, the occurrence of similar, fabric-preserving dolomitic ooids with fine crystal sizes at the onset of the Shuram excursion in the Johnnie oolite in southern California and Nevada, USA (Bergmann et al., 2011; Corsetti et al., 2006) suggests that perhaps the dolomite-precipitating conditions that formed the upper Khufai oolite were present on shallow carbonate shelves elsewhere ca. 574 million years ago. Notably, the ooid fabrics in the Johnnie Formation are more variably preserved likely due to the more significant burial and tectonic history of the Basin and Range province(Bergmann et al., 2011; Corsetti et al., 2006).

This model suggests that the kinetics of dolomite precipitation were favorable during upper Khufai time: high [Si], sulfur reducing bacteria, hypersalinity, high temperatures, and high [Mn] may have played a role in the precipitation of the dolomitic ooids we describe. Whether the ooid fabric we present in Figure 3 represents a unique dolomitic ooid morphology remains an open question; we encourage the use of PIC mapping to reveal the nanometer-scale crystal orientations of other fabric-preserving dolomites throughout Earth history.

Appendix A Materials and methods

A1 Sample preparation

All of the analyses described here were conducted on different parts of one hand sample (ca. 10 by 10 cm) of oolite collected by K. Bergmann from the upper Khufai Formation, Sultanate of Oman (MD6 258.6, see Bergmann et al. (2018); Osburn et al. (2014)). To prepare for PIC mapping, the sample was cut down to a 4mm^3 cube, polished and coated with 1nm of Pt following Sun et al. (2017). A second cut of the sample was thin sectioned, finished with a microprobe-quality polish to 0.25µm and carbon coated for electron probe spot analysis (Fig. 2b). For X-ray diffraction (Fig. 2c), a third section of the oolite sample was powdered using a drill press (Bergmann et al., 2018).

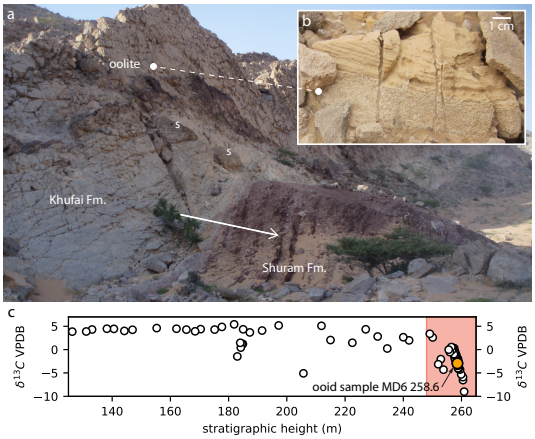

Figure 1. Khufai and Shuram Formations, Huqf outcrop area, Sultanate of Oman. **a:** Khufai Formation and overlying red silts of the Shuram Formation, as exposed in Mukhaibah Dome (see (Bergmann et al., 2018; Osburn et al., 2014)). Arrow points to stratigraphic up, 's' denote stromatolitic bioherms within the upper Khufai oolite, which is also labeled. **b:** Hand sample of the upper Khufai oolite showing cross-stratification within the ooid grainstone. K.D. Bergmann photos. **c:** Upper Khufai δ^{13}C curve from section MD6 in Osburn (2013). Data (three overlapping points) measured from the same oolite horizon we discuss herein are shown in the labeled orange circle. Red shading denotes the onset of the Shuram carbon isotope excursion.

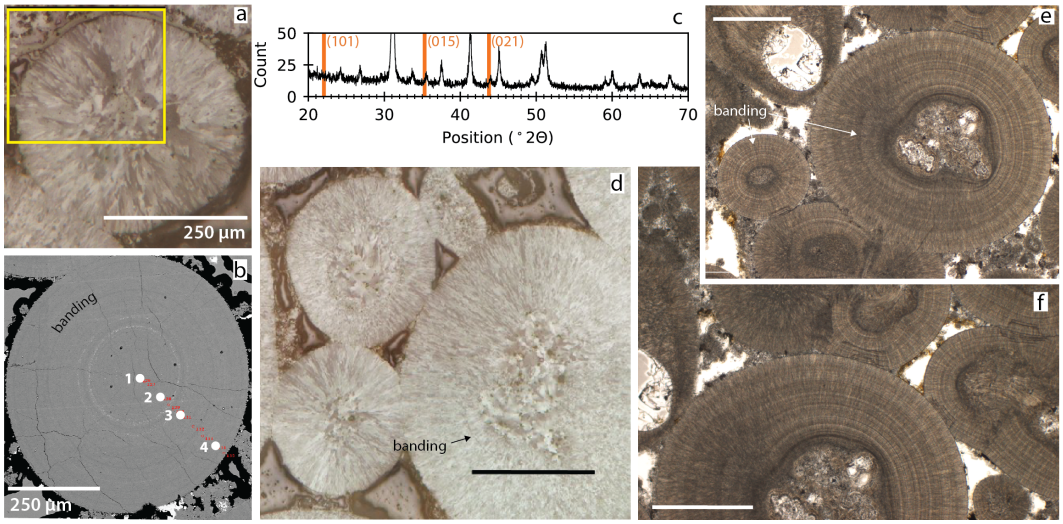

Figure 2. Petrographic images and mineralogy of the Khufai Formation oolite. **a:** Reflected light image. Yellow boxed region was PIC-mapped at 20µm resolution (shown in Figure 3a). **b:** Locations of electron probe micro analysis in a representative ooid within the upper Khufai oolite. Ca/Mg percent molar mass ratios in spots 1-4 are 21.8/13.2, 21.9/13.1, 22.3/12.7, and 21.8/13.0, respectively. **c:** XRD spectrum of the same oolite. Orange lines indicate dolomite ordering peaks (Kaczmarek et al., 2017). **d:** Reflected light image from the same hand sample as **a**. **e, f:** Thin section images of other ooids from the same bed in the upper Khufai Fm. Ooids in **d, e, f** all show the same novel dolomite crystal structure we observe and describe in detail for the ooid in **a** and Figure 3. Concentric banding, possibly due to intermittent abrasion during ooid formation (Anderson et al., 2020) is labeled. Scale bars are 500µm unless otherwise noted.

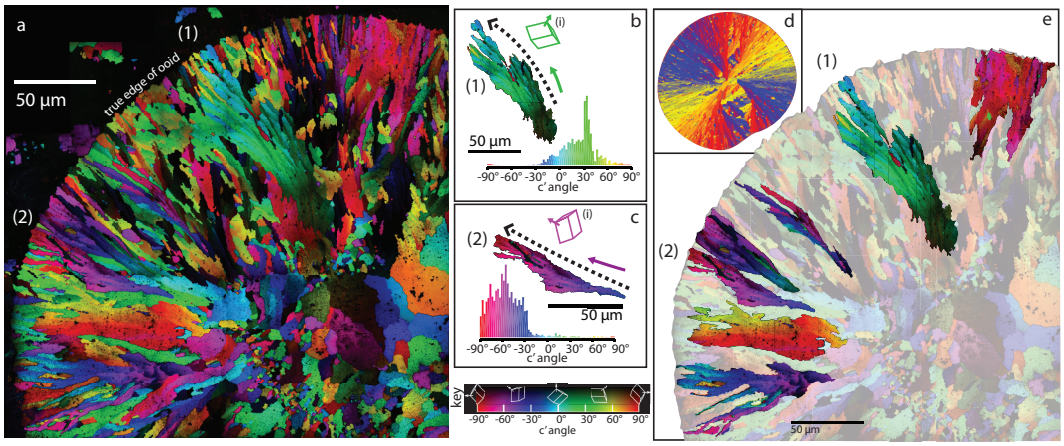

Figure 3. Crystal orientation maps of one fabric-preserving dolomitic ooid from the upper Khufai oolite. **a:** Polarization-dependent Imaging Contrast (PIC) map of the upper left quadrant of the ooid shown in Fig. 2a. Each region with one color corresponds to one crystal with a single crystal orientation. Colors and brightness represent in-plane and out-of-plane crystal c-axis orientations, respectively, as depicted by the dolomite rhombs and color bar (labeled "key"). The curved outer edge of the ooid is preserved; the black region in the upper left corner of this figure is void space filled with epoxy and with scattered, equant dolomite cements. **b, c:** Two bundles of similarly-oriented crystals extracted from the PIC map in **a**, **e** (labeled (1), (2)). Histograms of pixel colors within each bundle show that all crystals within each bundle are similarly oriented (within 60°, see Sun et al. (2017)). In each case, bundle elongation (dashed lines) and crystal length (solid arrows) are cooriented. Mode crystal orientation for each bundle is depicted by the sketched dolomite rhombs ((i), colored accordingly). The purple bundle, (2), is length-fast; the green bundle, (1), is length-slow. Bundles are curved, as shown by the gradient of color across each bundle. **d:** A modeled spherulitic form (Hendler et al., 2015) resembles the PIC map in A, including plumose bundles, abrupt misorientations, and bundles that terminate at the edge of the form. **e:** Highlighted view of some of the plumose, quasi-spherulitic bundles of similarly-oriented crystals observed in **a.**

A2 Polarization-dependent Imaging Contrast (PIC) Mapping

We collected the data displayed in the PIC map in Fig. 3 on beamline 11.0.1.1 at the Advanced Light Source, Lawrence Berkeley National Laboratory, using X-ray PhotoEmission Electron spectroMicroscopy (X-PEEM). The polished sample was mounted such that incident X-ray beams hit the sample at a 60° incident angle. Working at a fixed photon energy of 534 eV (π^* peak in carbonate oxygen K-edge spectra), the linear polarization was rotated at the undulator source from 0° to 90° in 5° increments. The resulting 19 images were stacked and analyzed using GG Macros (see Sun et al. (2017)). In each pixel of the stack, the intensity (I) vs. polarization angle (χ) curve was fit using a cosine-squared function: $I = a + bcos^2(\chi - c')$ (Malus's law) with three fit parameters – a, b and c' – where c' is the in-plane and b/a the out-of-plane angle of the crystal c-axis orientation, displayed, respectively, by by hue and brightness as shown by the color legend in Fig. 3 (Gilbert et al., 2011; DeVol et al., 2014). This process was repeated for a series of 56 by 56 µm areas, with 56nm pixels, partly overlapping to cover the entire quadrant of the ooid outlined in Fig. 2a. The $\sim$ 50 images were then stitched together using Adobe Photoshop CC 2017 to produce the PIC map shown in Fig. 3a. Together, the hue and brightness of each pixel in a PIC map completely describe the three-dimensional orientation of a crystal's c-axis at the same coordinates as the pixel.

A3 X-ray diffraction (XRD)

Oolite powder was analyzed on the PANalytical X'Pert Pro in the Material Science Department at the California Institute of Technology by Bergmann et al. (2018). Scans were run from 5-70° 2θ with a step size of 0.008 and a scan step time of 10.16 s. A Cu anode was used at 45 kV and 40 mA. A zero-background silicon plate was used for all measurements. Mineralogical phases were identified using the X'Pert Highscore IDMin function in Jade.

A4 Electron probe microanalysis (EPMA)

Electron probe spot analyses, shown in Fig. 2b, were taken using a JEOL JXA-8200 Electron Microprobe at the California Institute of Technology with an accelerating voltage of 15 kV, beam current of 20nA, and beam size of 1 µm. Non-quantitative elemental mapping was also conducted on the ooids to assess trace metal variability (Supplemental Figure 1). Calcite, dolomite and rhodochrosite standards were used to calibrate the Ca, Mg, and Mn measurements, respectively. Average detection limits for Ca, Mg and Mn were 177 ppm, 283 ppm, and 300 ppm respectively. The CITZAF method was used for matrix correction.

Acknowledgments

JW thanks C. Sun for help with sample preparation at UW-Madison and PIC mapping at the Advanced Light Source (ALS), and A. Maloof for comments on an early version of this manuscript. KDB thanks M. Osburn, J. Grotzinger and W. Fischer for field and laboratory support, and C. Ma for EPMA assistance. PG acknowledges 80% support from the U.S. DOE, Office of Science, Office of Basic Energy Sciences, Chemical Sciences, Geosciences, and Biosciences Division, under Award DE-FG02-07ER15899, and 20% support from NSF grant DMR-1603192. PEEM experiments were done at the ALS, supported by beamline scientist R. Chopdekar, and the Director, Office of Science, Office of Basic Energy Sciences, US DOE under Contract No. DE-AC02-05CH11231. Additional funding was provided by the Packard Foundation to KDB. The authors thank S. Kaczmarek for a helpful review. All new data (high-resolution PIC map, XRD spectrum, and EPMA spot analyses and elemental maps) are available in a Zenodo repository (DOI:10.5281/zenodo.5259649), or will be upon acceptance (applicable to the PIC map), and on Github (https://github.com/juliawilcots/synchrotron-paper-data) (Wilcots et al., 2021). The authors report no conflicts of interest.

References

Ahm, A.-S. C., & Husson, J. M. (2021). *Local and global controls on carbon isotope chemostratigraphy.* doi: https://doi.org/10.31223/X5V607

Anderson, N. T., Cowan, C. A., & Bergmann, K. D. (2020). A case for the growth of ancient ooids within the sediment pile. *Journal of Sedimentary Research*, *90*(8), 843–854.

Bergmann, K. D., Al Balushi, S. A. K., Mackey, T. J., Grotzinger, J. P., & Eiler, J. M. (2018). A 600-million-year carbonate clumped-isotope record from the Sultanate of Oman. *Journal of Sedimentary Research*, *88*(August), 960–979.

Bergmann, K. D., Zentmyer, R. A., & Fischer, W. W. (2011). The stratigraphic expression of a large negative carbon isotope excursion from the Ediacaran Johnnie Formation, Death Valley. *Precambrian Research*, *188*(1-4), 45–56.

Bjerrum, C. J., & Canfield, D. E. (2011, April). Towards a quantitative understanding of the late Neoproterozoic carbon cycle. *Proceedings of the National Academy of Sciences*, *108*(14), 5542-5547.

Bullen, S. B., & Sibley, D. F. (1984, November). Dolomite selectivity and mimic replacement. *Geology*, *12*, 655-658.

Cantine, M. D., Knoll, A. H., & Bergmann, K. D. (2020). Carbonates before skeletons: A database approach. *Earth-Science Reviews*, *201*, 103065.

Corsetti, F. A., Kidder, D. L., & Marenco, P. J. (2006). Trends in oolite dolomitization across the Neoproterozoic-Cambrian boundary: A case study from Death Valley, Cal-

ifornia. *Sedimentary Geology*, *191*(3-4), 135–150. doi: 10.1016/j.sedgeo.2006.03.021

Cui, H., Kaufman, A. J., Xiao, S., Zhou, C., Zhu, M., Cao, M., ... others (2021). Dynamic interplay of biogeochemical C, S, and Ba cycles in response to Shuram oxygenation event. *Journal of the Geological Society*.

Daye, M., Higgins, J., & Bosak, T. (2019). Formation of ordered dolomite in anaerobic photosynthetic biofilms. *Geology*, *47*(6), 509-512.

Derry, L. A. (2010). A burial diagenesis origin for the Ediacaran Shuram–Wonoka carbon isotope anomaly. *Earth and Planetary Science Letters*, *294*(1-2), 152–162.

DeVol, R. T., Metzler, R. A., Kabalah-Amitai, L., Pokroy, B., Politi, Y., Gal, A., ... others (2014). Oxygen spectroscopy and polarization-dependent imaging contrast (pic)-mapping of calcium carbonate minerals and biominerals. *The Journal of Physical Chemistry B*, *118*(28), 8449–8457.

Fang, Y., Hobbs, F. W., & Xu, H. (2021). Roles of dissolved silica in promoting abiotic precipitation of dolomite in the Great Salt Lake, Utah. In *Agu fall meeting 2021.*

Fang, Y., & Xu, H. (2022). Dissolved silica-catalyzed disordered dolomite precipitation. *American Mineralogist*. doi: https://doi.org/10.2138/am-2021-7474

Fang, Y., Zhang, F., Farfan, G. A., & Xu, H. (2021). Low-temperature synthesis of disordered dolomite and high-magnesium calcite in ethanolwater solutions: The solvation effect and implications. *ACS Omega*.

Fike, D. A., Grotzinger, J. P., Pratt, L., & Summons, R. E. (2006, December). Oxidation of the Ediacaran ocean. *Nature*, *444*, 744-747. doi: doi:10.1038/nature05345

Geyman, E. C., & Maloof, A. C. (2019). A diurnal carbon engine explains ^{13}c-enriched carbonates without increasing the global production of oxygen. *Proceedings of the National Academy of Sciences*, *116*(49), 24433–24439.

Gilbert, P. U. P. A., Young, A., & Coppersmith, S. N. (2011). Measurement of c-axis angular orientation in calcite (CaCO3) nanocrystals using X-ray absorption spectroscopy. *Proceedings of the National Academy of Sciences*, *108*(28), 11350–11355. doi: 10.1073/pnas.1107917108

Given, R. K., & Wilkinson, B. H. (1987). Dolomite abundance and stratigraphic age; constraints on rates and mechanisms of Phanerozoic dolostone formation. *Journal of Sedimentary Research*, *57*(6), 1068–1078.

Grotzinger, J. P., Fike, D. A., & Fischer, W. W. (2011, May). Enigmatic origin of the largest-known carbon isotope excursion in Earth's history. *Nature Geoscience*, *4*, 285-292.

Hendler, N., Mentovich, E., Korbuly, B., Pusztai, T., Gránásy, L., & Richter, S. (2015). Growth control of peptide-nanotube spherulitic films: Experiments and simulations. *Nano Research*, *8*(11), 3630–3638.

Hood, A. v. S., & Wallace, M. W. (2012). Synsedimentary diagenesis in a Cryogenian reef complex: Ubiquitous marine dolomite precipitation. *Sedimentary Geology*, *255-256*, 56-71.

Hood, A. v. S., & Wallace, M. W. (2018). Neoproterozoic marine carbonates and their paleoceanographic significance. *Global and Planetary Change*, *160*(November 2017), 28–45. doi: 10.1016/j.gloplacha.2017.11.006

Hood, A. v. S., Wallace, M. W., & Drysdale, R. N. (2011). Neoproterozoic aragonite-dolomite seas? Widespread marine dolomite precipitation in Cryogenian reef complexes. *Geology*, *39*(9), 871–874. doi: 10.1130/G32119.1

Husson, J. M., Linzmeier, B. J., Kitajima, K., Ishida, A., Maloof, A. C., Schoene, B., ... Valley, J. W. (2020). Large isotopic variability at the micron-scale in 'Shuram' excursion carbonates from South Australia. *Earth and Planetary Science Letters*, *538*(116211).

Kaczmarek, S. E., Gregg, J. M., Bish, D. L., Machel, H. G., & Fouke, B. W. (2017). Dolomite, very-high magnesium calcite, and microbes: implications for the microbial model of dolomitization. In A. MacNeil, J. Lonnee, & R. Wood (Eds.), *Characterization and Modeling of Carbonates–Mountjoy Symposium* (Vol. 1, pp. 7–20).

Knauth, L. P., & Kennedy, M. J. (2009, August). The late Precambrian greening of the Earth. *Nature*, *460*.

Osburn, M. (2013). *Isotopic Proxies for Microbial and Environmental Change: Insights from Hydrogen Isotopes and the Ediacaran Khufai Formation* (Unpublished doctoral dissertation). California Institute of Technology.

Osburn, M., Grotzinger, J., & Bergmann, K. (2014). Evolution of a middle Ediacaran carbonate ramp: Khufai Formation, Sultanate of Oman. *AAPG Bulletin*, *98*(8), 1631–1667. doi: 10.1306/07291312140

Rodriguez-Blanco, J. D., Shaw, S., & Benning, L. G. (2015). A route for the direct crystallization of dolomite. *American Mineralogist*, *100*(5-6), 1172–1181. doi: 10.2138/am-2015-4963

Rooney, A. D., Cantine, M. D., Bergmann, K. D., Gómez-pérez, I., & Al, B. (2020). Calibrating the coevolution of Ediacaran life and environment. *Proceedings of the National Academy of Sciences*, *117*(29), 16824–16830. doi: 10.1073/pnas.2002918117

Rothman, D. H., Hayes, J. M., & Summons, R. E. (2003, July). Dynamics of the Neoproterozoic carbon cycle. *Proceedings of the National Academy of Sciences*, *100*(14), 8124-8129.

Sandberg, P. A. (1975). New interpretations of Great Salt Lake ooids and of ancient non-skeletal carbonate mineralogy. *Sedimentology*, *22*, 497–537.

Schrag, D. P., Higgins, J. A., Macdonald, F. A., & Johnston, D. T. (2013, February).

Authigenic carbonate and the history of the global carbon cycle. *Science*, *339*, 540-543.

Sun, C.-Y., Gránásy, L., Stifler, C. A., Zaquin, T., Chopdekar, R. V., Tamura, N., ... others (2021). Crystal nucleation and growth of spherulites demonstrated by coral skeletons and phase-field simulations. *Acta Biomaterialia*, *120*, 277-292.

Sun, C. Y., Marcus, M. A., Frazier, M. J., Giuffre, A. J., Mass, T., & Gilbert, P. U. (2017). Spherulitic Growth of Coral Skeletons and Synthetic Aragonite: Nature's Three-Dimensional Printing. *ACS Nano*, *11*(7), 6612–6622. doi: 10.1021/acsnano.7b00127

Tarhan, L. G., Hood, A. v., Droser, M. L., Gehling, J. G., & Briggs, D. E. (2016, November). Exceptional preservation of soft-bodied ediacara biota promoted by silica-rich oceans. *Geology*, *44*(11), 951-954.

Trower, E. J., Lamb, M. P., & Fischer, W. W. (2017). Experimental evidence that ooid size reflects a dynamic equilibrium between rapid precipitation and abrasion rates. *Earth and Planetary Science Letters*, *468*, 112-118.

Tucker, M. E. (1982). Precambrian dolomites: Petrographic and isotopic evidence that they differ from Phanerozoic dolomites. *Geology*, *10*(January), 7–12.

Tucker, M. E. (1983, December). Diagenesis, geochemistry, and origin of a precambrian dolomite; the beck spring dolomite of eastern california. *Journal of Sedimentary Petrology*, *53*(4), 1097-1119.

Vasconcelos, C., & McKenzie, J. A. (1997). Microbial mediation of modern dolomite precipitation and diagenesis under anoxic conditions (lagoa vermelha, rio de janeiro, brazil). *Journal of sedimentary Research*, *67*(3), 378–390.

Vasconcelos, C., McKenzie, J. A., Bernasconi, S., Grujic, D., & Tiens, A. J. (1995). Microbial mediation as a possible mechanism for natural dolomite formation at low temperatures. *Nature*, *377*(6546), 220–222.

Vasconcelos, C., Warthmann, R., McKenzie, J. A., Visscher, P. T., Bittermann, A. G., & van Lith, Y. (2006). Lithifying microbial mats in Lagoa Vermelha, Brazil: modern Precambrian relics? *Sedimentary Geology*, *185*(3-4), 175–183.

Wacey, D., Wright, D. T., & Boyce, A. J. (2007). A stable isotope study of microbial dolomite formation in the Coorong Region, South Australia. *Chemical Geology*, *244*(1-2), 155–174.

Wilcots, J., Gilbert, P. U., & Bergmann, K. D. (2021, August). *juliawilcots/synchrotron-paper-data: Release for submission.* Zenodo. Retrieved from `https://doi.org/10.5281/zenodo.5259650` doi: 10.5281/zenodo.5259650

Wright, V. P., Ries, A. C., & Munn, S. G. (1990). Intraplatformal basin-fill deposits from the Infracambrian Huqf Group, east Central Oman. In A. Robertson, M. Shearle, &

A. Ries (Eds.), (p. 601-616). Geological Society of London.

Zempolich, W. G., & Baker, P. A. (1993). Experimental and natural mimetic dolomitization of aragonite ooids. *Journal of Sedimentary Research*, *63*(4), 596–606.

Zhang, F., Xu, H., Konishi, H., Kemp, J. M., Roden, E. E., & Shen, Z. (2012). Dissolved sulfide-catalyzed precipitation of disordered dolomite: Implications for the formation mechanism of sedimentary dolomite. *Geochimica et Cosmochimica Acta*, *97*, 148–165.

Supporting Information for "Nanoscale crystal fabric preserved in dolomite ooids at the onset of the Shuram Excursion"

Julia Wilcots[1], Pupa U. P. A. Gilbert[2], Kristin D. Bergmann[1]

[1]Department of Earth, Atmospheric and Planetary Sciences, Massachusetts Institute of Technology, Cambridge, MA

[2]Departments of Physics, Chemistry, Materials Science, Geoscience, University of Wisconsin, Madison, WI

Contents of this file

1. Figure S1 and S2

Additional Supporting Information (Files uploaded separately)

1. Table S1

Introduction

Included in this file are (1) additional crystal orientation maps and histograms of the PIC mapped ooid displayed in Figure 3 of the main text (Figure S2), and (2) additional elec-

Corresponding author:

Julia Wilcots,

Department of Earth, Atmospheric and Planetary Science,

Massachusetts Institute of Technology, Cambridge, MA. (jwilcots@mit.edu)

tron probe microanalysis elemental maps and spot analysis measurements to accompany Figure 2b in the main text (Figure S1 and Table S1). Table S1 can be downloaded as a separate spreadsheet. Crystal orientatons were measured by J. Wilcots, K.D. Bergmann, and P.U.P.A. Gilbert over the course of two beamtime sessions in April and November 2018 on beamline 11.0.1.1 at the Advanced Light Source, Lawrence Berkeley National Laboratory, using X-ray PhotoEmission Electron spectroMicroscopy (X-PEEM). Bundles were selected manually in Adobe Photoshop, after the ooid PIC map (Figure 3a) was produced. The color (orientation) of each pixel within each bundle are plotted in histograms. EPMA results were collected by K.D. Bergmann in November 2011 at the California Institute of Technology. All figures and data are stored in a Zenodo repository (DOI:10.5281/zenodo.5259649; Wilcots, Gilbert, and Bergmann (2021)).

References

Wilcots, J., Gilbert, P. U., & Bergmann, K. D. (2021, August). *juliawilcots/synchrotron-paper-data: Release for submission.* Zenodo. Retrieved from `https://doi.org/10.5281/zenodo.5259650` doi: 10.5281/zenodo.5259650

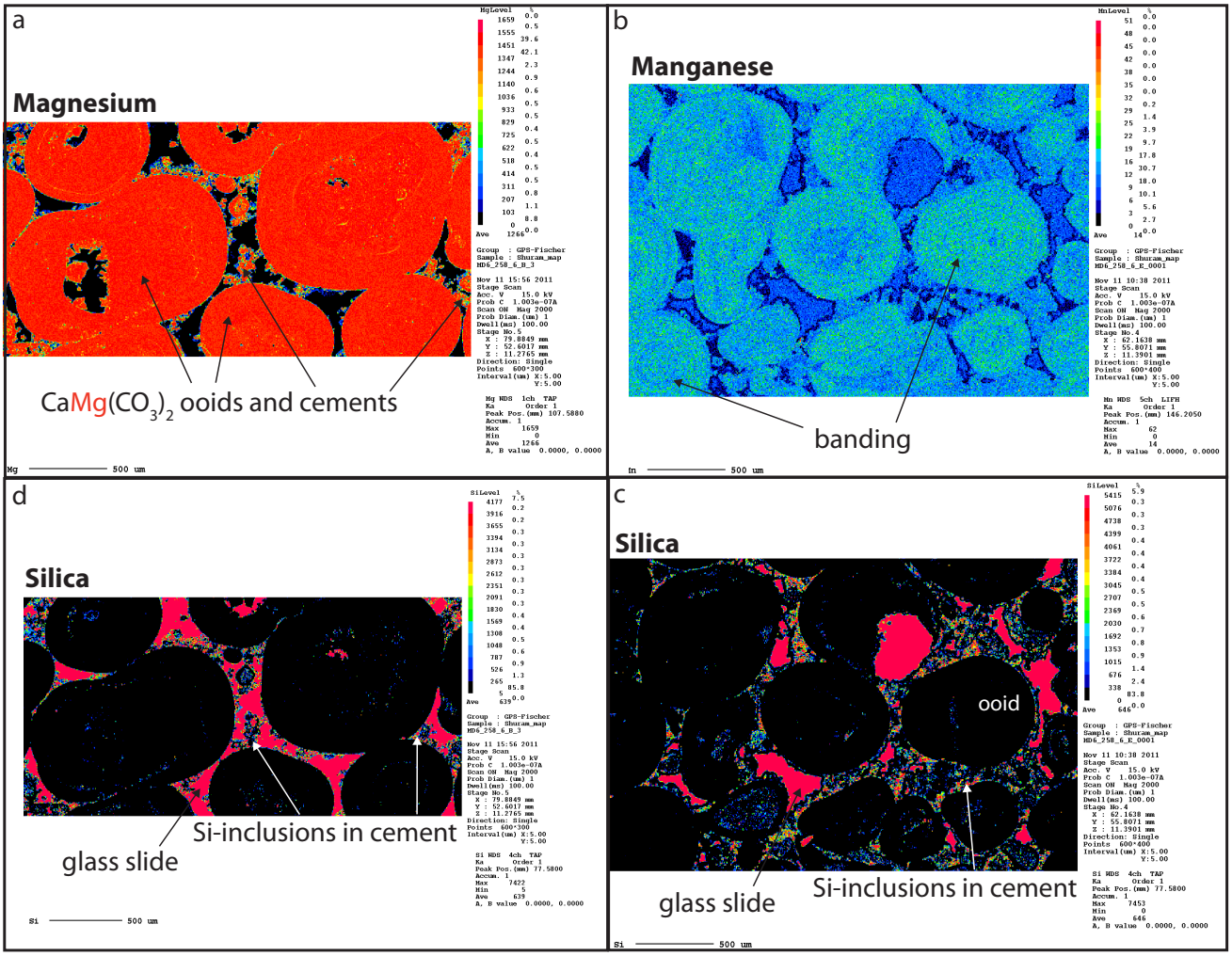

Figure S1. Elemental maps of two thin sections of the upper Khufai oolite. **a** and **d** show Mg and Si in sample MD6 258.6 B3 (see Table S1), respectively. **b** and **c** show Mn and Si in sample MD6 258.6 e1 (Table S1).

Table S1. Electron probe microanalyses (EPMA) collected by K.D. Bergmann on Nov. 16 2011. Methods are described in the main text and the data file is available as a separate file.

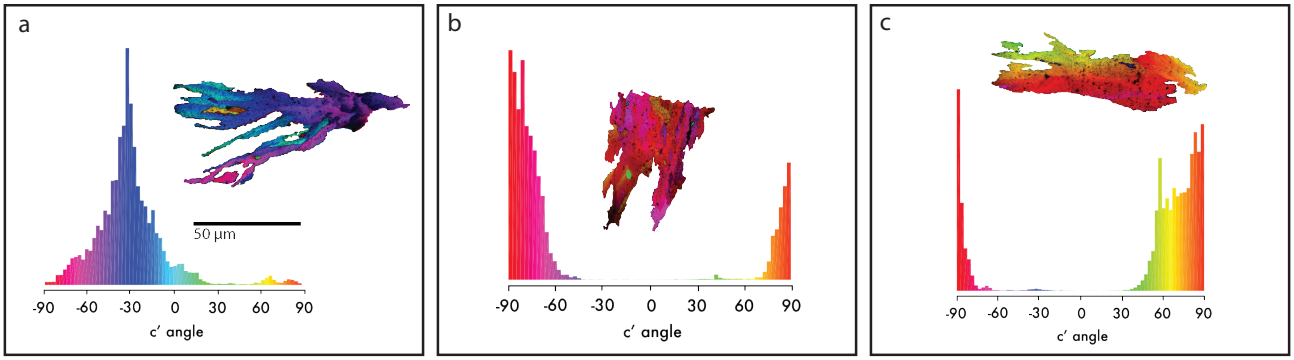

Figure S2. Histograms of crystal orientations within three bundles highlighted in Figure 3e of the main text. Like the two bundles displayed in Figure 3b,c of the main text, crystals within these bundles are co-oriented within $\sim 60°$ within in bundle. Each bundle is plotted in its original orientation.